

Probing Dark Photons from Nuclear De-excitation in Reactor Neutrino Experiment

Yuanchao Lou^{1,*} and Lei Wu^{1,2,†}

¹*Department of Physics and Institute of Theoretical Physics,
Nanjing Normal University, Nanjing, 210023, China*

²*Nanjing Key Laboratory of Particle Physics and Astrophysics, Nanjing, 210023, China*

Reactor neutrino experiments serve as powerful probes of light new physics. We investigate MeV-scale visible dark photons (A') produced in nuclear reactors through nuclear de-excitation following neutron capture $N^* \rightarrow NA'$. Compared with the conventional Compton-like production process $\gamma e^- \rightarrow A' e^-$, the nuclear de-excitation yields on-shell dark photons with masses up to the nuclear transition energy. Using data from the TEXONO CsI(Tl) detector, we derive the new constraints on the kinetic mixing parameter ϵ for dark photon masses in the range $0.1 \text{ MeV} < m_{A'} < 6.9 \text{ MeV}$. We find that nuclear de-excitation not only extends the mass reach of reactor searches to higher dark photon masses but also provides a stronger limit than the Compton-like production process.

I. INTRODUCTION

Despite compelling gravitational evidence for dark matter, its particle identity remains unknown [1, 2]. Recent years have seen growing interest in sub-GeV “light” dark matter. Thermal freeze-out in this mass range generally requires new light mediators, with the dark photon being a leading candidate [3–11]. Arising from a $U(1)_D$ gauge symmetry, the dark photon can mix with the Standard Model photon at the $\sim 10^{-3}$ to 10^{-6} level, providing a minimal mechanism for efficient annihilation. These considerations strongly motivate dedicated low-energy probes of dark photons. Such a light vector mediator can connect ordinary matter to MeV-scale dark-sector states and can appear in viable freeze-out or freeze-in dark matter scenarios [12–16].

Fixed-target experiments have constrained dark photons through either visible-decay signatures, including Orsay, KEK, E137, E141, E774, APEX, and HPS [17–25], or missing-energy signatures, such as NA64 [26, 27], with related searches also carried out at fixed-target configurations and Belle II [28, 29]. These searches exclude kinetic mixings roughly in the range $\epsilon \sim 10^{-5}$ – 10^{-3} for MeV-to-GeV dark photons depending on the experimental channel. Collider searches, including BaBar and KLOE-2, probe dark photons produced in e^+e^- collisions and set limits on ϵ for similar mass ranges [30–33], while long-lived dark photon signatures at the LHC have also been explored [34], and accelerator-based dark photon searches have been reviewed in [35]. Low-threshold direct detection experiments provide constraints on light dark photons at sub-MeV masses [36, 37]. Astrophysical and cosmological probes provide additional constraints from stellar cooling, supernova emission, BBN, and ΔN_{eff} [38–46].

Nuclear reactors offer an alternative laboratory source of MeV-scale weakly coupled particles through their intense photon environment, and have recently been ex-

plored for axion-like particle searches in near-reactor detectors [47–49] and for boosted dark matter via reactor neutron scattering [50]. The conventional Compton-like production process $\gamma e^- \rightarrow A' e^-$ in reactor materials produces a flux of dark photons detectable in nearby reactor neutrino detectors, yielding constraints on ϵ for $m_{A'} \lesssim 1 \text{ MeV}$ [51]. A subsequent reanalysis with the proper treatment of photon–hidden-photon oscillations in the reactor medium was discussed in Ref. [52]. However, the dark photon produced from such a channel is limited by two-body kinematics, which requires $m_{A'} \leq \sqrt{m_e^2 + 2m_e E_\gamma} - m_e$, such as $m_{A'}^{\text{max}} \sim 3.0 \text{ MeV}$ for a typical reactor photon energy $E_\gamma = 12 \text{ MeV}$. The rapid high-energy falloff of the reactor photon spectrum [53], $dN_\gamma/dE_\gamma \sim \exp(-1.1 E_\gamma/\text{MeV})$ further limits the practical reach.

In this work, we investigate the visible dark photons produced in nuclear reactors through the neutron-capture nuclear de-excitation. Different from the continuum emission of Compton-like processes, this mechanism provides a discrete line source of dark photons. When a nucleus N absorbs a thermal neutron and reaches an excited state N^* , it can de-excite either by emitting an ordinary photon or, via kinetic mixing, a dark photon A' [54]. We note that the emitted dark photon carries energy $E_{A'} \simeq \omega_i$, set by the nuclear transition energy, allowing on-shell production of dark photon whenever $m_{A'} < \omega_i$. Consequently, nuclear de-excitation lifts the kinematic limit of Compton-like production, allowing reactor experiments to probe dark photons up to the nuclear transition energy. Here, we consider the representative electric dipole transition (E1) from $^{238}\text{U}(n, \gamma)^{239}\text{U}$ and $^{10}\text{B}(n, \gamma)^{11}\text{B}$ processes. For completeness, the Compton-like source is also included below its kinematic endpoint. The produced dark photons are searched for through the visible decay $A' \rightarrow e^+e^-$ and inverse Compton-like scattering $A'e^- \rightarrow \gamma e^-$ inside the detector. This paper is organized as follows. In Sec. II we describe the two production mechanisms and compute the dark photon flux at the reactor. Section III discusses the visible-decay and inverse Compton-like detection channels. We present our constraints in Sec. IV and compare with existing bounds.

* yuanchao'lou@nnu.edu.cn

† leiwu@njnu.edu.cn

Section V summarizes our conclusions.

II. DARK-PHOTON PRODUCTION AT NUCLEAR REACTORS

The dark photon A' is the massive gauge boson associated with a hidden $U(1)_D$ gauge group. Its Lagrangian, including kinetic and mass terms as well as couplings to the SM electromagnetic current, is given by

$$\mathcal{L} = -\frac{1}{4}F'_{\mu\nu}F'^{\mu\nu} + \frac{1}{2}m_{A'}^2 A'_\mu A'^\mu - \epsilon e A'_\mu J_{\text{EM}}^\mu, \quad (1)$$

where $F'_{\mu\nu} = \partial_\mu A'_\nu - \partial_\nu A'_\mu$ is the dark photon field strength tensor, $m_{A'}$ is the dark photon mass, which may be generated, for example, by a dark Higgs mechanism [9] or by a Stueckelberg mechanism [55, 56], ϵ is the kinetic-mixing parameter, and $J_{\text{EM}}^\mu = \sum_f Q_f \bar{f} \gamma^\mu f$ is the SM electromagnetic current summed over all charged fermions f with electric charge Q_f .

Neutron-capture nuclear de-excitation provides an important production channel of dark photon in the reactors. After neutron capture, an excited nuclear state N^* can de-excite by emitting an on-shell dark photon through the kinetic mixing with the SM photon,

$$n + N \rightarrow N^* \rightarrow N + A'. \quad (2)$$

Since nuclear recoil corrections are negligible at MeV scales, the emitted dark photon from the i -th transition line carries energy $E_{A',i} \simeq \omega_i$, where ω_i is the corresponding transition energy, and can be produced whenever $m_{A'} < \omega_i$. The dark-photon flux at the detector from the i -th transition is given by

$$\Phi_{A',i} = \frac{\dot{N}_{\gamma,i} r_i}{4\pi L^2}, \quad (3)$$

and the total de-excitation flux is $\Phi_{A'}^{\text{deex}} = \sum_i \Phi_{A',i}$. Here r_i is the dark-photon-to-photon emission ratio for the same transition line,

$$r_i = \frac{\sigma(n + N \rightarrow N^* \rightarrow N + A')}{\sigma(n + N \rightarrow N^* \rightarrow N + \gamma)}. \quad (4)$$

For an electric dipole transition of energy ω_i , this ratio evaluates to [57]

$$r_{E1,i} = \epsilon^2 \left(1 + \frac{m_{A'}^2}{2\omega_i^2}\right) \sqrt{1 - \frac{m_{A'}^2}{\omega_i^2}} \Theta(\omega_i - m_{A'}). \quad (5)$$

We consider representative E1 transitions from $^{238}\text{U}(n, \gamma)^{239}\text{U}$ and $^{10}\text{B}(n, \gamma)^{11}\text{B}$. The selected transitions and their energies are listed in Table I. The highest retained transition is the 7.007 MeV E1 line from $^{10}\text{B}(n, \gamma)^{11}\text{B}$; however, the available phase space $\sqrt{1 - m_{A'}^2/\omega_i^2}$ vanishes as $m_{A'} \rightarrow \omega_i$, and the dark-photon flux becomes negligibly small before reaching this endpoint. We therefore restrict the scan to $m_{A'} \leq$

6.9 MeV, just below the kinematic limit set by the highest transition energy. We note that the sensitivity for $m_{A'}$ above the uranium transition energies is substantially reduced by the small $^{10}\text{B}(n, \gamma)$ branching factor, as discussed below.

TABLE I. Radiative neutron-capture transitions used in this work, with reaction, transition energy ω_i , multipolarity, photon intensity I_γ per 100 radiative captures, and radiative-capture branching factor $f_{n\gamma}$.

Reaction	ω_i [MeV]	Type	I_γ	$f_{n\gamma}$
$^{238}\text{U}(n, \gamma)^{239}\text{U}$	3.297	E1	13.21	1
$^{238}\text{U}(n, \gamma)^{239}\text{U}$	4.060	E1	6.95	1
$^{10}\text{B}(n, \gamma)^{11}\text{B}$	4.711	E1	25.58	7.9×10^{-5}
$^{10}\text{B}(n, \gamma)^{11}\text{B}$	7.007	E1	55.10	7.9×10^{-5}

The ordinary photon emission rate for transition i from capture isotope N is given by

$$\dot{N}_{\gamma,i} = N_n \frac{Y_n^{(N)}}{\sum_N Y_n^{(N)}} f_{n\gamma}^{(N)} \frac{I_\gamma^{(N, \omega_i)}}{100}, \quad (6)$$

where N_n is the total neutron production rate, $Y_n^{(N)}$ is the neutron-absorption yield per fission for isotope N , $I_\gamma^{(N, \omega_i)}$ is the number of photons of energy ω_i emitted per 100 radiative captures, and $f_{n\gamma}^{(N)}$ is the fraction of neutron absorptions proceeding via the radiative-capture channel. We take $f_{n\gamma}^{(238\text{U})} = 1$, since radiative capture dominates for ^{238}U . For ^{10}B , the dominant absorption channel is $^{10}\text{B}(n, \alpha)^7\text{Li}$ with thermal cross section 3837 b, while $\sigma[^{10}\text{B}(n, \gamma)^{11}\text{B}] \simeq 0.305$ b, giving $f_{n\gamma}^{(10\text{B})} \simeq 7.9 \times 10^{-5}$ [58]. The total neutron production rate N_n is determined by the reactor thermal power. Each fission releases an average of 200 MeV energy [59] and produces 2.5 neutrons on average [60], giving $N_n = 7.8 \times 10^{19} \times P$, where P is the reactor thermal power in GW. For the TEXONO configuration with $P = 2.9$ GW, this yields $N_n \simeq 2.3 \times 10^{20} \text{ s}^{-1}$. The neutron-absorption yields and transition intensities are taken from Refs. [60, 61].

For the nuclear de-excitation contribution, we focus on the dark photons emitted directly in the primary transition $N^* \rightarrow NA'$. Ordinary transition photons may also propagate through reactor materials and subsequently produce dark photons through secondary Compton-like conversion, $\gamma e^- \rightarrow A' e^-$. Such a component would require a reactor-specific photon-transport treatment, including the geometry, material composition, and attenuation history of the photons, and is not included here.

The continuum Compton-like contribution is treated separately using the reactor photon spectrum. We adopt the analytical parametrization obtained for the FRJ-1 reactor core, which applies for photon energies $E_\gamma \gtrsim 200$ keV [53].

$$\frac{d\dot{N}_\gamma}{dE_\gamma} = 5.8 \times 10^{17} \frac{1}{\text{MeV} \cdot \text{s}} \frac{P}{\text{MW}} e^{-1.1E_\gamma/\text{MeV}}. \quad (7)$$

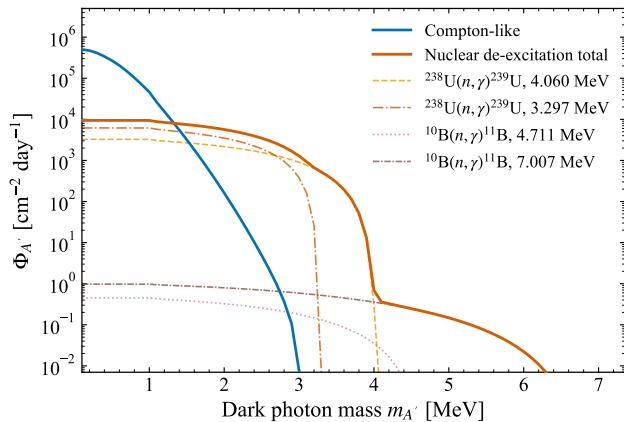


FIG. 1. Integrated dark-photon flux $\Phi_{A'}$ at the TEXONO detector as a function of dark-photon mass $m_{A'}$, for $\epsilon = 10^{-6}$. The blue curve shows the Compton-like flux, obtained by integrating $d\Phi_{A'}/dE_{A'}$ over all energies, which closes at $m_{A'}^{\max} = 3.03$ MeV. The dashed and dash-dotted curves show individual de-excitation line contributions from $^{238}\text{U}(n, \gamma)^{239}\text{U}$ (3.297 and 4.060 MeV E1) and $^{10}\text{B}(n, \gamma)^{11}\text{B}$ (4.711 and 7.007 MeV E1), and the orange curve gives their sum. The de-excitation channel extends reactor sensitivity to $m_{A'} \lesssim 6.9$ MeV, well beyond the Compton-like ceiling.

This spectrum is dominated by prompt fission γ -rays and covers energies up to several MeV. The resulting dark-photon flux at the detector is

$$\frac{d\Phi_{A'}^{\text{comp}}}{dE_{A'}} = \frac{1}{4\pi L^2} \int dE_\gamma \frac{d\dot{N}_\gamma}{dE_\gamma} \frac{1}{\sigma_{\text{tot}}(E_\gamma)} \frac{d\sigma_{\gamma e \rightarrow A'e}}{dE_{A'}}, \quad (8)$$

where $L = 28$ m is the reactor-to-detector distance for TEXONO [62]. The factor $(1/\sigma_{\text{tot}}) d\sigma_{\gamma e \rightarrow A'e}/dE_{A'}$ is the differential probability for a reactor photon interaction to produce a dark photon with energy $E_{A'}$. We take $\sigma_{\text{tot}}(E_\gamma) = \sigma_{\text{SM}}(E_\gamma) + \sigma_{\gamma e \rightarrow A'e}(E_\gamma) \simeq \sigma_{\text{SM}}(E_\gamma)$, since the dark-photon production cross section is suppressed by $\epsilon^2 \ll 1$. The SM cross section $\sigma_{\text{SM}}(E_\gamma)$ is taken from the XCOM photon cross-section database [63].

Figure 1 shows the integrated dark-photon flux $\Phi_{A'}$ as a function of dark-photon mass $m_{A'}$ for $\epsilon = 10^{-6}$, where the Compton-like flux is included for comparison as the energy-integrated total $\Phi_{A'}^{\text{Compton}} = \int dE_{A'} d\Phi_{A'}/dE_{A'}$. The individual de-excitation lines (dashed and dash-dotted curves) each contribute a flat plateau that terminates sharply at $m_{A'} = \omega_i$, while the total de-excitation flux (orange) extends to $m_{A'} \lesssim 6.9$ MeV, well beyond the mass endpoint of the dark photon from the Compton-like process, $m_{A'} = 3.03$ MeV.

III. DETECTION AND EVENT RATES

The TEXONO CsI(Tl) detector is located at the Kuo-Sheng Reactor Neutrino Laboratory, $L = 28$ m from

a $P = 2.9$ GW reactor core [62]. The detector has a total mass $M_{\text{det}} = 187$ kg, and we use the TEXONO analysis window $3 \text{ MeV} < E_{\text{dep}} < 8 \text{ MeV}$. The number of target electrons per unit detector mass is $N_e/M_{\text{det}} = 108 N_A/M_{\text{CsI}} \simeq 2.51 \times 10^{26} \text{ kg}^{-1}$, where $M_{\text{CsI}} = 259.81 \text{ g mol}^{-1}$ and 108 is the number of electrons per CsI formula unit.

Dark photons arriving at the detector can give two visible signatures: decay inside the detector, $A' \rightarrow e^+e^-$, and inverse Compton-like scattering on electrons, $A'e^- \rightarrow \gamma e^-$. For visible decays, the partial width is

$$\Gamma_{A' \rightarrow e^+e^-} = \frac{\epsilon^2 \alpha m_{A'}}{3} \left(1 + \frac{2m_e^2}{m_{A'}^2}\right) \sqrt{1 - \frac{4m_e^2}{m_{A'}^2}}, \quad (9)$$

for $m_{A'} > 2m_e$. The boosted decay length is

$$\ell_{A'}(E_{A'}) = \frac{p_{A'}}{m_{A'} \Gamma_{A' \rightarrow e^+e^-}}, \quad (10)$$

where $p_{A'} = \sqrt{E_{A'}^2 - m_{A'}^2}$. Numerically, $\ell_{A'} \sim 4 \times 10^{10} \text{ m} (\epsilon/10^{-6})^{-2} (m_{A'}/\text{MeV})^{-2} (E_{A'}/\text{MeV})$, which far exceeds the baseline for the TEXONO configuration in the coupling and mass range of interest. The survival probability $P_{\text{surv}}(L, E_{A'}) = \exp[-L/\ell_{A'}(E_{A'})]$ is close to unity throughout most of the parameter space considered here; we nevertheless retain this factor in the numerical calculation. For decays inside the detector, the visible energy is $E_{\text{dep}} \simeq E_{A'}$.

For inverse Compton-like scattering [64], we compute the lab-frame differential cross section $d\sigma_{A'e \rightarrow \gamma e}/dE_r$, where E_r is the outgoing photon energy. The squared matrix element and the kinematic transformation to the lab frame are summarized in Appendix A. Assuming full containment of the final-state photon and electron, energy conservation gives $E_{\text{dep}} \simeq E_r + T_e = E_{A'}$, where T_e is the recoil electron kinetic energy. As a consistency check, in the limit $m_{A'} \ll m_e$ our result reduces to

$$\frac{d\sigma_{A'e \rightarrow \gamma e}}{dE_r} \simeq \frac{2}{3} \epsilon^2 \frac{d\sigma_C}{dE_r} \left[1 + \mathcal{O}\left(\frac{m_{A'}^2}{m_e^2}\right)\right], \quad (11)$$

in agreement with the approximation used in Ref. [51].

Having specified the two detection channels, we now write the corresponding event-rate expressions for the two reactor production sources. For the continuous Compton-like source, the scattering contribution per unit detector mass is

$$\frac{dR_{\text{scat}}^{\text{comp}}}{dE_{A'}} = \frac{N_e}{M_{\text{det}}} \frac{d\Phi_{A'}^{\text{comp}}}{dE_{A'}} \sigma_{A'e \rightarrow \gamma e}(E_{A'}), \quad (12)$$

where

$$\sigma_{A'e \rightarrow \gamma e}(E_{A'}) = \int_{E_r^{\min}}^{E_r^{\max}} dE_r \frac{d\sigma_{A'e \rightarrow \gamma e}}{dE_r}. \quad (13)$$

The corresponding visible-decay contribution in the long-lived limit is

$$\frac{dR_{\text{dec}}^{\text{comp}}}{dE_{A'}} \simeq \frac{V_{\text{det}}}{M_{\text{det}}} \frac{d\Phi_{A'}^{\text{comp}}}{dE_{A'}} \frac{P_{\text{surv}}(L, E_{A'})}{\ell_{A'}(E_{A'})}, \quad (14)$$

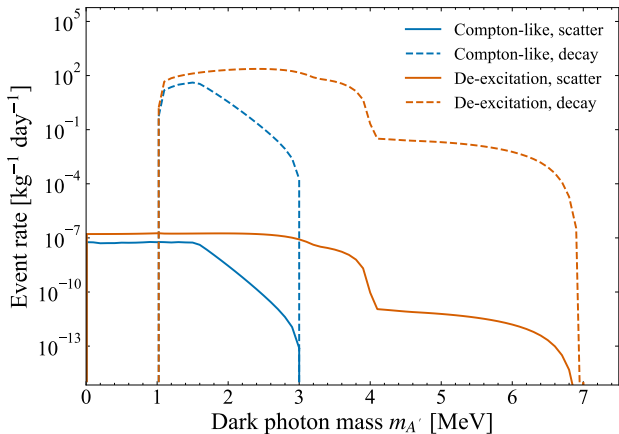


FIG. 2. Event-rate components at the TEXONO CsI detector for $\epsilon = 10^{-6}$. Solid curves show inverse Compton-like scattering $A'e^- \rightarrow \gamma e^-$; dashed curves show visible decays $A' \rightarrow e^+e^-$. Blue and orange curves correspond to Compton-like production and nuclear de-excitation, respectively.

where V_{det} is the active detector volume.

For the nuclear de-excitation source, the emitted dark photons are monoenergetic, $E_{A',i} \simeq \omega_i$. The scattering rate per unit detector mass from line i is

$$R_{\text{scat},i}^{\text{deex}} = \frac{N_e}{M_{\text{det}}} \Phi_{A',i} \sigma_{A'e \rightarrow \gamma e}(\omega_i), \quad (15)$$

while the visible-decay rate is

$$R_{\text{dec},i}^{\text{deex}} \simeq \frac{V_{\text{det}}}{M_{\text{det}}} \Phi_{A',i} \frac{P_{\text{surv}}(L, \omega_i)}{\ell_{A'}(\omega_i)}. \quad (16)$$

Figure 2 compares the scattering and decay rate components for the two reactor production mechanisms. The Compton-like contribution follows the continuum reactor photon flux, whereas the de-excitation contribution reflects the selected nuclear transition lines. In the parameter point shown, the visible-decay contribution dominates once $A' \rightarrow e^+e^-$ is kinematically open.

IV. CONSTRAINTS

We constrain the two visible signatures with different TEXONO CsI(Tl) observables. For visible decays, $A' \rightarrow e^+e^-$, we use the TEXONO three-hit cosmic-ray-unrelated pair-production spectrum, which selects one primary energy deposition accompanied by two 511 keV annihilation photons in neighboring crystals [62]. For inverse Compton-like scattering, $A'e^- \rightarrow \gamma e^-$, we instead use the inclusive TEXONO $\bar{\nu}_e - e^-$ measurement in the same energy window, requiring the predicted scattering contribution to satisfy $N_{\text{scat}} < N_{\text{scat}}^{95} = 1.96 \times 100.6 \simeq 197.2$ at 95% C.L. At each mass point, the final limit on

ϵ is taken as the stronger of the two constraints; in practice, the scattering constraint dominates below the e^+e^- threshold and the visible-decay constraint above it.

For the Compton-like source, the dark-photon spectrum is continuous in $E_{A'}$. The number of inverse Compton-like scattering events is obtained by integrating the predicted deposited-energy spectrum over the TEXONO analysis window,

$$N_{\text{scat}}^{\text{comp}} = M_{\text{det}} T \int_{3 \text{ MeV}}^{8 \text{ MeV}} dE_{A'} \frac{dR_{\text{scat}}^{\text{comp}}}{dE_{A'}}, \quad (17)$$

where $T = 160$ days. Parameter points satisfying $N_{\text{scat}}^{\text{comp}} > N_{\text{scat}}^{95}$ are excluded. The same Compton-produced dark-photon flux can also give visible decays inside the detector. This contribution is compared with the TEXONO three-hit pair-production spectrum. The predicted binned decay rate is

$$\left(\frac{dR_{\text{dec}}^{\text{comp}}}{dE} \right)_b = \frac{1}{\Delta E_b} \int_{E_b^{\text{min}}}^{E_b^{\text{max}}} dE_{\text{dep}} \frac{dR_{\text{dec}}^{\text{comp}}}{dE_{\text{dep}}}, \quad (18)$$

where $dR_{\text{dec}}^{\text{comp}}/dE_{\text{dep}}$ is obtained from Eq. (14). We use a bin-wise χ^2 statistic,

$$\chi_{\text{dec}}^2(\epsilon) = \sum_b \left[\frac{\max(0, (dR_{\text{dec}}^{\text{comp}}/dE)_b - R_b^{\text{obs}})}{\sigma_b} \right]^2, \quad (19)$$

where R_b^{obs} and σ_b are the measured central value and experimental uncertainty in bin b of the TEXONO three-hit cosmic-ray-unrelated pair-production spectrum. The 95% C.L. upper limit is obtained from $\Delta\chi^2 = 3.84$.

For the nuclear de-excitation source, the dark photons are produced as monoenergetic lines with $E_{A',i} \simeq \omega_i$. The inverse Compton-like scattering contribution is treated with the inclusive TEXONO event-count constraint,

$$N_{\text{scat}}^{\text{deex}} = M_{\text{det}} T \sum_i R_{\text{scat},i}^{\text{deex}} \Theta(3 \text{ MeV} < \omega_i < 8 \text{ MeV}), \quad (20)$$

where $R_{\text{scat},i}^{\text{deex}}$ is the scattering event rate per unit detector mass from line i . Parameter points satisfying $N_{\text{scat}}^{\text{deex}} > N_{\text{scat}}^{95}$ are excluded. The same de-excitation flux can also produce visible decays inside the detector. Since this signal is line-like, we compare it with the TEXONO three-hit pair-production spectrum using a bin-by-bin rate cap. The decay rate $R_{\text{dec},i}^{\text{deex}}$ for line i is converted into a bin-averaged differential rate,

$$\mathcal{R}_b^{\text{deex}} = \frac{1}{\Delta E_b} \sum_{i \in b} R_{\text{dec},i}^{\text{deex}}, \quad (21)$$

where the sum runs over all de-excitation lines whose transition energies fall in bin b . We conservatively exclude a parameter point if $\mathcal{R}_b^{\text{deex}}$ exceeds the corresponding TEXONO three-hit cosmic-ray-unrelated rate cap in any bin containing a de-excitation line, following the conservative recast strategy of Ref. [54].

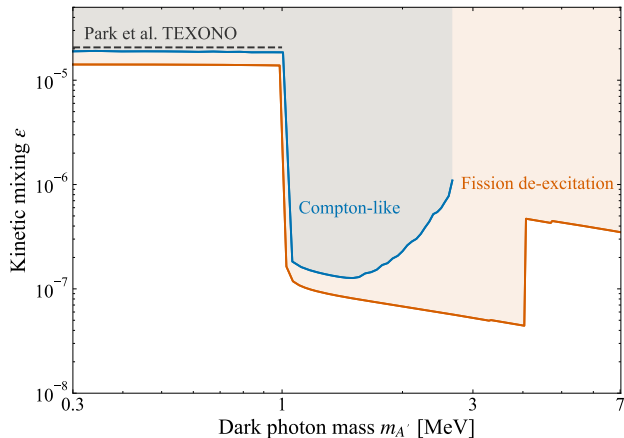


FIG. 3. Constraints on the kinetic mixing parameter ϵ as a function of dark-photon mass $m_{A'}$, derived from the TEXONO CsI(Tl) data. The blue curve shows the constraint from Compton-like reactor production, combining the inclusive TEXONO event-count constraint for inverse Compton-like scattering with the H3 pair-production recast for visible decays. The orange curve shows the corresponding constraint from neutron-capture nuclear de-excitation, where the line-like visible-decay signal is treated with a conservative bin-cap procedure. The gray reference line shows the previous TEXONO reactor Compton-like limit of Ref. [51].

Figure 3 shows the resulting TEXONO constraints in the $(m_{A'}, \epsilon)$ plane. For each production mechanism, the inverse Compton-like scattering contribution is constrained using the inclusive TEXONO $\bar{\nu}_e - e^-$ event count limit, while visible decays are constrained using the TEXONO three-hit pair production data. For the continuous Compton-like source, the visible decay contribution is recast with an upper-only binned χ^2 . For the monoenergetic nuclear de-excitation source, the line-like visible-decay contribution is constrained with the conservative lower envelope bin cap procedure. The two reactor sources probe qualitatively different regions of phase space. The Compton-like contribution is controlled by the high-energy tail of the reactor photon spectrum and rapidly loses support near its kinematic endpoint. In contrast, neutron-capture de-excitation provides localized dark photon sources at discrete nuclear transition energies. The resulting constraint therefore reflects a set of line-like probes, with the strongest sensitivity occurring when an intense transition falls inside the TEXONO analysis window and contributes to either the inclusive scattering constraint or the three-hit visible decay constraint.

It is useful to compare the reactor constraints with other probes. Beam-dump experiments such as E137 constrain dark photons produced in high-energy electromagnetic showers over macroscopic baselines [22, 23]; their sensitivity depends on the production rate, shielding survival, and detector geometry, probing a distinct regime from the short-baseline MeV-scale reactor source consid-

ered here. Astrophysical and cosmological bounds from stellar cooling, supernovae, BBN, and ΔN_{eff} can be powerful, but depend on in-medium production, trapping, and the thermal history of the dark sector [38, 40, 43, 45]. The reactor constraints derived here instead are based on measured reactor and detector inputs, without invoking astrophysical or cosmological assumptions.

V. CONCLUSION

We have studied MeV-scale visible dark photons produced at nuclear reactors through two mechanisms. The first is Compton-like conversion of reactor photons on electrons, $\gamma e^- \rightarrow A' e^-$, which produces a continuous dark photon spectrum but is kinematically limited to $m_{A'} \lesssim 3$ MeV for the reactor photon energies relevant to TEXONO. The second is neutron-capture nuclear de-excitation, $N^* \rightarrow N A'$, in which an on-shell dark photon is emitted in place of an ordinary transition photon. Since this process is controlled by discrete nuclear transition energies, it can extend the reactor dark-photon source above the Compton-like endpoint.

Using selected E1 transitions from $^{238}\text{U}(n, \gamma)^{239}\text{U}$ and $^{10}\text{B}(n, \gamma)^{11}\text{B}$, we computed the corresponding dark-photon flux at the TEXONO detector. We considered two visible detection signatures in the CsI(Tl) array: inverse Compton-like scattering, $A' e^- \rightarrow \gamma e^-$, and visible decay, $A' \rightarrow e^+ e^-$. The scattering contribution was constrained using the inclusive TEXONO $\bar{\nu}_e - e^-$ event-count measurement in the 3–8 MeV deposited-energy window, while the visible decay contribution was constrained using the TEXONO three-hit pair-production spectrum. This treatment separates the two experimental topologies and allows both continuous Compton-like sources and discrete nuclear de-excitation lines to be tested consistently.

The resulting limits constrain the kinetic mixing parameter ϵ in the MeV-scale mass range. Beyond extending the mass coverage, the key physics point is that reactor neutron capture provides a calibrated line source of on-shell dark photons, tying the reactor sensitivity to measured nuclear transition energies and intensities rather than to the exponentially suppressed high-energy tail of the continuum photon spectrum.

These limits provide an independent laboratory probe of MeV-scale visible dark photons, distinct from accelerator beam-dump, astrophysical, and cosmological constraints. Beam-dump experiments probe dark photons produced in high-energy electromagnetic showers and are sensitive to the interplay of production, shielding, propagation, and detector geometry. Astrophysical and cosmological bounds can be powerful, but depend on assumptions about in-medium production, trapping, thermal history, and available decay modes.

The reactor constraints derived here are instead based on measured reactor and detector inputs, without invoking astrophysical or cosmological assumptions. Further

improvements can come from a more complete set of neutron-capture transitions and from applying the same strategy to high-resolution near-reactor detectors, such as TAO [65], which could strengthen the sensitivity to line-like de-excitation signals. The same production formalism can also be adapted to invisible dark-photon decays sourcing light dark matter via reactor de-excitation.

ACKNOWLEDGMENTS

We thank Maxim Pospelov for helpful discussions. L.W. is supported by the NNSFC under Grant No. 12275134 and No. 12335005.

Appendix A: Kinematics for the Inverse Compton-like Process

In this appendix we summarize the kinematic expressions used to compute the inverse Compton-like detection process,

$$A'(p_1) + e^-(p_2) \rightarrow \gamma(k_1) + e^-(k_2), \quad (\text{A1})$$

with the initial electron at rest in the laboratory frame. The Mandelstam variable is

$$s = m_e^2 + m_{A'}^2 + 2m_e E_{A'}, \quad (\text{A2})$$

where $E_{A'}$ is the lab-frame dark-photon energy. We define the dimensionless ratios

$$x_e \equiv \frac{m_e}{\sqrt{s}}, \quad x_{A'} \equiv \frac{m_{A'}}{\sqrt{s}}, \quad (\text{A3})$$

and

$$\kappa = \frac{1}{2} \sqrt{(1 + x_e^2 - x_{A'}^2)^2 - 4x_e^2}. \quad (\text{A4})$$

The center-of-mass energy of the outgoing photon is

$$E_\gamma^* = \frac{s - m_e^2}{2\sqrt{s}}. \quad (\text{A5})$$

After averaging over initial-state polarizations and summing over final-state polarizations, the COM-frame differential cross section can be written as

$$\frac{d\sigma_{A'e \rightarrow \gamma e}}{d\Omega^*} = \frac{\alpha^2 \epsilon^2}{48s} \frac{1 - x_e^2}{\kappa} (T_1 + T_2 + T_3), \quad (\text{A6})$$

where

$$T_1 = \frac{16}{(1 - x_e^2)^2} \left[2x_e^4 + x_e^2(1 - x_e^2) + x_e^2 x_{A'}^2 - \frac{1}{2}(1 - x_e^2)\eta \right], \quad (\text{A7})$$

$$T_2 = \frac{16}{(1 - x_e^2)\eta} \left[x_e^2(1 - x_e^2) + x_e^2\eta + 4x_e^4 + x_{A'}^2(1 - x_e^2 - x_{A'}^2 + \eta) \right], \quad (\text{A8})$$

$$T_3 = \frac{16}{\eta^2} \left[2x_e^4 + x_e^2\eta + x_e^2 x_{A'}^2 - \frac{1}{2}(1 - x_e^2)\eta \right]. \quad (\text{A9})$$

where

$$\eta = x_{A'}^2 - \frac{1}{2}(1 + x_e^2)(1 - x_e^2 + x_{A'}^2) - \kappa(1 - x_e^2) \cos \theta^*. \quad (\text{A10})$$

Here θ^* is the COM-frame angle of the outgoing photon with respect to the incoming dark-photon direction.

To obtain the lab-frame differential cross section with respect to the outgoing photon energy, we boost from the COM frame to the lab frame. The boost parameters are

$$\beta_{\text{cm}} = \frac{p_{A'}^{\text{lab}}}{E_{A'} + m_e}, \quad \gamma_{\text{cm}} = \frac{E_{A'} + m_e}{\sqrt{s}}, \quad (\text{A11})$$

where

$$p_{A'}^{\text{lab}} = \sqrt{E_{A'}^2 - m_{A'}^2}. \quad (\text{A12})$$

The lab-frame photon energy is

$$E_r = \gamma_{\text{cm}} E_\gamma^* (1 + \beta_{\text{cm}} \cos \theta^*), \quad (\text{A13})$$

so that

$$\cos \theta^*(E_r) = \frac{1}{\beta_{\text{cm}}} \left[\frac{E_r}{\gamma_{\text{cm}} E_\gamma^*} - 1 \right]. \quad (\text{A14})$$

The kinematically allowed lab-frame energy range is therefore

$$E_r^{\text{min}} = \gamma_{\text{cm}} E_\gamma^* (1 - \beta_{\text{cm}}), \quad E_r^{\text{max}} = \gamma_{\text{cm}} E_\gamma^* (1 + \beta_{\text{cm}}). \quad (\text{A15})$$

Using

$$d\Omega^* = 2\pi d \cos \theta^*, \quad \frac{d \cos \theta^*}{dE_r} = \frac{1}{\gamma_{\text{cm}} \beta_{\text{cm}} E_\gamma^*}, \quad (\text{A16})$$

we obtain

$$\frac{d\sigma_{A'e \rightarrow \gamma e}}{dE_r} = \frac{2\pi}{\gamma_{\text{cm}} \beta_{\text{cm}} E_\gamma^*} \frac{d\sigma_{A'e \rightarrow \gamma e}}{d\Omega^*} \Bigg|_{\cos \theta^* = \cos \theta^*(E_r)}. \quad (\text{A17})$$

This expression is used in the event-rate calculation in Sec. III.

[1] N. Aghanim *et al.* (Planck), *Astron. Astrophys.* **641**, A6 (2020), [Erratum: *Astron. Astrophys.* 652, C4 (2021)],

- [2] G. Bertone, D. Hooper, and J. Silk, *Phys. Rept.* **405**, 279 (2005), [arXiv:hep-ph/0404175](#).
- [3] B. Holdom, *Phys. Lett. B* **166**, 196 (1986).
- [4] L. B. Okun, *Sov. Phys. JETP* **56**, 502 (1982).
- [5] N. Arkani-Hamed, D. P. Finkbeiner, T. R. Slatyer, and N. Weiner, *Phys. Rev. D* **79**, 015014 (2009), [arXiv:0810.0713 \[hep-ph\]](#).
- [6] J. D. Bjorken, R. Essig, P. Schuster, and N. Toro, *Phys. Rev. D* **80**, 075018 (2009), [arXiv:0906.0580 \[hep-ph\]](#).
- [7] J. Jaeckel and A. Ringwald, *Ann. Rev. Nucl. Part. Sci.* **60**, 405 (2010), [arXiv:1002.0329 \[hep-ph\]](#).
- [8] R. Essig *et al.*, in *Snowmass 2013: Snowmass on the Mississippi* (2013) [arXiv:1311.0029 \[hep-ph\]](#).
- [9] M. Fabbri, E. Gabrielli, and G. Lanfranchi, *The Dark Photon* (Springer, 2021) [arXiv:2005.01515 \[hep-ph\]](#).
- [10] A. Caputo, A. J. Millar, C. A. J. O'Hare, and E. Vitagliano, *Phys. Rev. D* **104**, 095029 (2021), [arXiv:2105.04565 \[hep-ph\]](#).
- [11] J. Alexander *et al.* (2016) [arXiv:1608.08632 \[hep-ph\]](#).
- [12] C. Boehm and P. Fayet, *Nucl. Phys. B* **683**, 219 (2004), [hep-ph/0305261](#).
- [13] J. L. Feng and J. Kumar, *Phys. Rev. Lett.* **101**, 231301 (2008), [0803.4196](#).
- [14] F. Compagnin, S. Profumo, and N. Fornengo, *JCAP* **03**, 012, [arXiv:2211.13825 \[hep-ph\]](#).
- [15] T. Nomura and X. Xu, *Chin. Phys. C* **49**, 063104 (2025), [arXiv:2405.17885 \[hep-ph\]](#).
- [16] S. Knapen, T. Lin, and K. M. Zurek, *Phys. Rev. D* **96**, 115021 (2017), [1709.07882](#).
- [17] M. Davier and H. Nguyen Ngoc, *Phys. Lett. B* **229**, 150 (1989).
- [18] A. Konaka *et al.*, *Phys. Rev. Lett.* **57**, 659 (1986).
- [19] J. D. Bjorken, S. Ecklund, W. R. Nelson, A. Abashian, C. Church, B. Lu, L. W. Mo, T. A. Nunamaker, and P. Rassmann, *Phys. Rev. D* **38**, 3375 (1988).
- [20] E. M. Riordan *et al.*, *Phys. Rev. Lett.* **59**, 755 (1987).
- [21] A. Bross, M. Crisler, S. Pordes, J. Volk, S. Errede, and J. Wrbanek, *Phys. Rev. Lett.* **67**, 2942 (1991).
- [22] L. Marsicano, M. Battaglieri, M. Bondi, C. D. R. Carvalho, A. Celentano, M. De Napoli, R. De Vita, E. Nardi, M. Raggi, and P. Valente, *Phys. Rev. D* **98**, 015031 (2018), [arXiv:1802.03794 \[hep-ex\]](#).
- [23] B. Batell, R. Essig, and Z. Surujon, *Phys. Rev. Lett.* **113**, 171802 (2014), [arXiv:1406.2698 \[hep-ph\]](#).
- [24] S. Abrahamyan *et al.* (APEX), *Phys. Rev. Lett.* **107**, 191804 (2011), [arXiv:1108.2750 \[hep-ex\]](#).
- [25] O. Moreno and M. Solt (HPS), *PoS ICHEP2018*, 076 (2019), [arXiv:1812.02169 \[hep-ex\]](#).
- [26] D. Banerjee *et al.*, *Phys. Rev. Lett.* **123**, 121801 (2019), [arXiv:1906.00176 \[hep-ex\]](#).
- [27] D. Banerjee *et al.* (NA64), *Phys. Rev. Lett.* **118**, 011802 (2017), [arXiv:1610.02988 \[hep-ex\]](#).
- [28] S.-F. Ge, J. Liang, Z. Liu, and U. Min, *Dark Photon Searches with Initial-State Radiation at Fixed-Target Configurations* (2025), [arXiv:2505.10302 \[hep-ph\]](#).
- [29] J. Liang, Z. Liu, and L. Yang, *JHEP* **05**, 273, [arXiv:2212.04252 \[hep-ph\]](#).
- [30] J. P. Lees *et al.* (BaBar), *Phys. Rev. Lett.* **113**, 201801 (2014), [arXiv:1406.2980 \[hep-ex\]](#).
- [31] F. Archilli *et al.* (KLOE-2), *Phys. Lett. B* **706**, 251 (2012), [arXiv:1110.0411 \[hep-ex\]](#).
- [32] D. Babusci *et al.* (KLOE-2), *Phys. Lett. B* **720**, 111 (2013), [arXiv:1210.3927 \[hep-ex\]](#).
- [33] A. Anastasi *et al.* (KLOE-2), *Phys. Lett. B* **757**, 356 (2016), [arXiv:1603.06086 \[hep-ex\]](#).
- [34] M. Du, Z. Liu, and V. Q. Tran, *JHEP* **05**, 055, [arXiv:1912.00422 \[hep-ph\]](#).
- [35] M. Graham, C. Hearty, and M. Williams, *Ann. Rev. Nucl. Part. Sci.* **71**, 37 (2021), [arXiv:2104.10280 \[hep-ph\]](#).
- [36] H. An, M. Pospelov, and J. Pradler, *Phys. Rev. Lett.* **111**, 041302 (2013), [arXiv:1304.3461 \[hep-ph\]](#).
- [37] T. Li *et al.* (PandaX), *Phys. Rev. Lett.* **134**, 071004 (2025), [arXiv:2409.00773 \[hep-ex\]](#).
- [38] H. An, M. Pospelov, and J. Pradler, *Phys. Lett. B* **725**, 190 (2013), [arXiv:1302.3884 \[hep-ph\]](#).
- [39] J. Redondo and G. Raffelt, *JCAP* **08**, 034, [arXiv:1305.2920 \[hep-ph\]](#).
- [40] J. H. Chang, R. Essig, and S. D. McDermott, *JHEP* **01**, 107, [arXiv:1611.03864 \[hep-ph\]](#).
- [41] E. Rrapaj and S. Reddy, *Phys. Rev. C* **94**, 045805 (2016), [arXiv:1511.09136 \[nucl-th\]](#).
- [42] E. Hardy and R. Lasenby, *JHEP* **02**, 033, [arXiv:1611.05852 \[hep-ph\]](#).
- [43] M. Ibe, S. Kobayashi, Y. Nakayama, and S. Shirai, *JHEP* **04**, 009, [arXiv:1912.12152 \[hep-ph\]](#).
- [44] P. Arias, D. Cadamuro, M. Goodsell, J. Jaeckel, J. Redondo, and A. Ringwald, *JCAP* **06**, 013, [arXiv:1201.5902 \[hep-ph\]](#).
- [45] A. Fradette, M. Pospelov, J. Pradler, and A. Ritz, *Phys. Rev. D* **99**, 075004 (2019), [arXiv:1812.07585 \[hep-ph\]](#).
- [46] M. Hufnagel, K. Schmidt-Hoberg, and S. Wild, *JCAP* **11**, 032, [arXiv:1808.09324 \[hep-ph\]](#).
- [47] W. Dai, Y. Gong, G. Gu, L. Su, L. Wang, L. Wu, Y. Wu, and L. Yang, *Hunting for Axions in REactor neutrino COherent scattering Detection Experiment* (2025), [arXiv:2509.01538 \[hep-ph\]](#).
- [48] Y. Gong, J. Guo, N. Liu, L. Su, and W.-N. Yang, *Detecting Axion-like Particles with Plasmon in Reactor-based Experiment* (2026), [arXiv:2601.07448 \[hep-ph\]](#).
- [49] Y. Shen, J. Tang, L. Wang, Y. Wu, and L. Yang, *Sensitivity of the RECODE Reactor CEvNS Experiment to the Dark Axion Portal* (2026), [arXiv:2603.24050 \[hep-ph\]](#).
- [50] Y. Ema, M. Pospelov, and A. Ray, *JHEP* **07**, 094, [arXiv:2402.03431 \[hep-ph\]](#).
- [51] H. Park, *Phys. Rev. Lett.* **119**, 081801 (2017), [arXiv:1705.02470 \[hep-ph\]](#).
- [52] M. Danilov, S. Demidov, and D. Gorbunov, *Phys. Rev. Lett.* **122**, 041801 (2019), [arXiv:1804.10777 \[hep-ph\]](#).
- [53] H. Bechteler, H. Faissner, R. Yogeshwar, and H. Seyfarth, *The spectrum of gamma radiation emitted in the FRJ-1 (Merlin) reactor core and moderator region*, Tech. Rep. Juel-Spez-255 (Kernforschungsanlage Jülich, 1984).
- [54] T. Gao and M. Pospelov, *Constraints on millicharged particles from nuclear gamma-decays* (2025), [arXiv:2507.17955 \[hep-ph\]](#).
- [55] D. Feldman, Z. Liu, and P. Nath, *Phys. Rev. D* **75**, 115001 (2007), [arXiv:hep-ph/0702123](#).
- [56] D. Feldman, Z. Liu, and P. Nath, *AIP Conf. Proc.* **939**, 50 (2007), [arXiv:0705.2924 \[hep-ph\]](#).
- [57] C. Pitrou and M. Pospelov, *Phys. Rev. C* **102**, 015803 (2020), [arXiv:1904.07795 \[astro-ph.CO\]](#).
- [58] S. F. Mughabghab, *Atlas of Neutron Resonances: Resonance Parameters and Thermal Cross Sections, Z = 1–100*, 5th ed. (Elsevier, Amsterdam, 2006).
- [59] N. Schunck, *Nuclear Fission: Theories, Experiments and Applications* (Springer, 2024).
- [60] B. Xin *et al.* (TEXONO), *Phys. Rev. D* **72**, 012006 (2005), [arXiv:hep-ex/0502001](#).

- [61] National Nuclear Data Center, Evaluated Nuclear Structure Data File (ENSDF), <https://www.nndc.bnl.gov/ensdf/> (2024), accessed: 2024.
- [62] M. Deniz *et al.* (TEXONO), *Phys. Rev. D* **81**, 072001 (2010), [arXiv:0911.1597](https://arxiv.org/abs/0911.1597) [hep-ex].
- [63] Xcom: Photon cross sections database, <https://physics.nist.gov/PhysRefData/Xcom/html/xcom1.html> (2010).
- [64] L. Su, L. Wu, and B. Zhu, *Phys. Rev. D* **105**, 055021 (2022), [arXiv:2105.06326](https://arxiv.org/abs/2105.06326) [hep-ph].
- [65] A. Abusleme *et al.* (JUNO), TAO Conceptual Design Report: A Precision Measurement of the Reactor Antineutrino Spectrum with Sub-percent Energy Resolution (2020), [arXiv:2005.08745](https://arxiv.org/abs/2005.08745) [physics.ins-det].